

# 1 **Phase-specific pooling of sparse assembly activity by respiration-related brain oscillations**

2 Shani Folschweiller & Jonas-Frederic Sauer\*

3

4 Institute of Physiology I, Medical Faculty, Albert-Ludwigs-University Freiburg, Hermann-Herder-Straße 7,  
5 79104 Freiburg, Germany

6

7 \*correspondence should be addressed to: [jonas.sauer@physiologie.uni-freiburg.de](mailto:jonas.sauer@physiologie.uni-freiburg.de)

8

## 9 **Summary**

10 Nasal breathing affects cognitive functions, but it has remained largely unclear how respiration-  
11 driven inputs shape information processing in neuronal circuits. Current theories emphasize the  
12 role of neuronal assemblies, coalitions of transiently active pyramidal cells, as the core unit of  
13 cortical network computations. Here, we show that respiration-related oscillations (RROs) directly  
14 pace the activation of neuronal assemblies in the medial prefrontal cortex (mPFC) of mice.  
15 Neuronal assemblies are more efficiently entrained than single neurons and activate preferentially  
16 during the descending phase of RROs. At the same time, overlap between individual assemblies is  
17 minimized during descending RRO due to the efficient recruitment of GABAergic neurons by  
18 assemblies. Our results thus suggest the RROs support cortical operations by defining time  
19 windows of enhanced yet segregated assembly activity.

20

## 21 **Key words:**

22 Neuronal assembly, respiration, respiration-driven oscillations, prefrontal cortex, embodied  
23 cognition

## Introduction

Nasal airflow activates olfactory sensory neurons in the olfactory epithelium (Grosmaître et al., 2007), thereby producing oscillating depolarizations that are broadcast to the brain via the olfactory bulbs (Fontanini and Bower, 2006). Besides the well-studied role of respiration-related oscillations (RROs) in the processing of olfactory information (Kay, 2015), converging evidences indicate that RROs occurs in a variety of higher-order cortical areas including the medial prefrontal cortex (mPFC, Biskamp et al., 2017, Nguyen Chi et al., 2016, Lockmann et al., 2016, Ito et al., 2014, Zhong et al., 2017, Karalis and Sirota, 2018, Moberly et al., 2018, Kőszeghy et al., 2018, Bagur et al., 2021). These results suggest that rhythmic breathing might affect cognitive functions beyond the processing of smells (Heck et al., 2019). Behavioural studies on human participants indeed demonstrated that nasal respiration supports memory encoding and recall (Zelano et al., 2016, Nakamura et al., 2018, Arshamian et al., 2018), but how respiration affects information processing and fundamental circuit operations in higher-order neocortex has remained largely unexplored on the mechanistic level.

Neuronal assemblies are thought to comprise the building blocks of cognitive function (Buzsáki, 2010, Papadimitriou et al., 2020, El-Gaby et al., 2021). Assemblies are composed of co-active neurons which transiently and consistently fire together, and are thought to convey information to downstream reader neurons by effective synaptic transmission due to their synchronized activity (Buzsáki, 2010). The recurrent nature of connections among cortical pyramidal cells and strengthening of connections of coactive neurons are thought to provide the structural and functional grounds for the emergence of assemblies (Harris, 2005, Palm et al., 2014). One way in which RROs could impact cortical information processing is to directly modulate the activity of assemblies. Focusing on the medial prefrontal cortex (mPFC), a highly associative brain area providing top-down control to cortex (Le Merre et al., 2021), we tested this hypothesis in awake mice. We find that assembly patterns emerge during spontaneous behaviour in the mPFC, and that these patterns are entrained by ongoing RROs. Assembly patterns preferentially activate during the descending phase of the RRO, when cortical excitation is maximized. Moreover, we provide evidence that the differential recruitment of putative GABAergic interneurons by

assemblies during the descending phase of RRO supports the temporal segregation of assembly patterns. These results thus suggest that rhythmic breathing affects cognitive function at a fundamental level by defining time windows of preferred assembly activation.

## Results

### Prefrontal assemblies are entrained by respiration-related oscillations

The cortical local field potential (LFP) is characterized by prominent RROs, which peak in the 1-5 Hz frequency band during immobility (Biskamp et al., 2017, Zhong et al., 2017, Karalis and Sirota, 2018). We confirmed this finding in head-fixed mice, in which we simultaneously recorded LFP signals from the olfactory epithelium (LFP<sub>olf</sub>) and the mPFC (Karalis and Sirota, 2018, Fig. 1A,B). During immobility, the mPFC LFP showed a spectral peak at ~1-5 Hz, which coincided with high spectral power of the LFP<sub>olf</sub> (Fig. 1C,D). Furthermore, we found both signals to be coherent in the 1-5 Hz band (Fig. 1E). 1-5 Hz LFP power (Fig. 1C,F) and coherence with respiration moreover showed a dorso-ventral increase, consistent with a previous report on RROs in the mPFC (Karalis and Sirota, 2018, Fig. 1E,H). Our data thus support recent accounts that 1-5 Hz oscillatory activity in the mPFC reflects primarily a respiration-related rhythm. During movement, power spectra of both cortical LFP and respiration peaked at ~7-10 Hz (Supplementary Fig. 1). Given the spectral overlap to theta oscillations in mice (~7 Hz), it was less clear to what extent 7-10 Hz LFP oscillations were driven by respiration during movement. We thus focused on immobile states to assess the potential impact of 1-5 Hz RROs on neuronal assemblies.

Motivated by previous reports of spontaneously occurring cell assemblies in neocortex and hippocampus (Peyrache et al., 2009, Miller et al., 2014, El-Gaby et al., 2021), we screened for assembly patterns in a dataset of single unit recordings from the mPFC of head-fixed, awake mice navigating in a virtual arena. In this paradigm, the animals showed periods of voluntary locomotion intermingled with extended epochs of immobility (proportion immobility:  $0.40 \pm 0.03$ ,  $n=13$  mice). We identified neuronal assembly activations from the occurrence of co-firing of neurons exceeding random coactivation (25 ms bin width,  $60 \pm 4$  neurons per session, Fig. 2A, Supplementary Fig 2, Lopes-dos-Santos et al., 2013). This approach reliably extracted cell assemblies in simulated data

(Supplementary Fig. 2) and identified on average one assembly pattern per  $6.8 \pm 0.2$  neurons in the mPFC data set (25 sessions from 13 mice, 1494 pyramidal cells in total), similar to results from the hippocampus (El-Gaby et al., 2021). Assembly patterns were dominated by few neurons with large weights, which displayed more strongly correlated spike trains than neurons with low weight ( $p=10^{-131}$ , Fig. 2A, see Supplementary Fig. 3 for additional quantification of assembly parameters). Ongoing network activity in the mPFC is thus characterized by the emergence of spontaneously activating neuronal assemblies.

To quantify the expression of assembly patterns with high temporal resolution, we extracted for each pattern the time course of activation by projecting the weight vectors on smoothed spike trains of all simultaneously recorded pyramidal neurons (Fig. 2B,C, van de Ven et al., 2016). We extracted all RRO cycles during which a given pattern activated, and quantified the number of assembly activations as a function of RRO phase. Importantly, since the duration of each phase bin is taken into account, this analysis is robust against waveform asymmetries of the RRO. Comparison against randomly shuffled onset times for each pattern revealed that 38 % of identified assembly patterns were significantly entrained by the ongoing RRO (84 out of 221 patterns,  $n=13$  mice, Fig. 2D). The majority of patterns activated during the descending phase of RRO, thus coinciding with excitation of the circuitry during negative LFP deflections (Fig. 2D). This finding was robust against different threshold values for the detection of active assemblies (Supplementary Fig. 4). Considering all 221 patterns, we detected a significantly higher activation frequency and stronger average expression strength during the descending compared to the ascending phase ( $p=4.8 \cdot 10^{-11}$  and  $p=6.0 \cdot 10^{-6}$ , Fig. 2E). These data thus demonstrate that RRO defines time windows of preferred activity for neuronal ensembles.

### **RRO entrainment of assemblies emerges despite variable coupling of contributing neurons**

We next asked whether the entrainment of assembly patterns by rhythmic breathing is a reflection of the functional grouping of highly RRO-coupled neurons into assemblies, or whether it is an emergent property that is independent from the RRO-coupling of the contributing neurons. We found evidence for the latter: First, the mean coupling strength of patterns was higher than that of

individual neurons ( $p=6 \times 10^{-20}$ , Fig. 2F). Second, the average RRO coupling intensity of neurons with high contribution to assembly patterns did not differ from low-contributing neurons ( $p=0.648$ , Fig. 2G), indicating that coactivity of pyramidal cells with varying RRO coupling depth underlies RRO-paced assemblies. Third, correlation of a neuron's weight in the assembly with the RRO coupling intensity of that neuron was generally low and showed no significant difference for RRO-entrained and non-entrained patterns ( $p=0.063$ , Fig. 2H). Thus, it is the transient coactivation of assemblies which is entrained by respiration, independently of the coupling of the individual neurons forming them.

### **RRO-paced interneuron activity supports sparse assembly activations**

Given that assemblies activate more often during the descending phase of RR, we next asked whether this results in enhanced assembly overlap due to an increase in co-occurrence by chance. We quantified the coactivation of any two simultaneously recorded patterns within a time window of  $\pm 10$  ms, which is within the integration time of cortical neurons (Koch et al., 1996). Despite higher assembly frequency (Fig. 2E), we observed reduced coactivation during the descending compared to the ascending phase (Fig. 3A,  $n=931$  pairs of patterns,  $p=0.004$ ). These data suggest that active mechanisms contribute to keeping assembly activations apart from each other during descending RRO.

Previous work showed that GABAergic interneurons associate their activity with individual assembly patterns (Dupret et al., 2013). Feedback inhibition by GABAergic cells that are recruited by some but not other assemblies might thus provide a mechanism to maintain a sparse assembly activation profile (Buzsáki, 2010). For this to be true, interneurons should be differentially recruited by individual assembly patterns, fire when assemblies activate, and be more strongly aligned with assemblies during the descending phase of RRO. To test these predictions, we analyzed electrophysiologically identified interneurons that were recorded simultaneously with the pyramidal cell population ( $n=270$  putative interneurons). We found that interneurons showed diverse activity profiles (i.e. firing change in relation to the onset of each assembly pattern, Fig. 3B). The similarity in interneuron profiles between two patterns correlated positively with the coactivation strength of

the same pair of patterns (Fig. 3C, Spearman's  $r=0.358$ ,  $p=3 \times 10^{-29}$ ), indicating that strongly coactivating patterns share similar interneuron profiles. Moreover, similar to assembly patterns, interneurons discharged more during the descending phase of RRO (Fig. 3D). Finally, interneurons showed stronger coactivation with the assembly patterns during the descending than the ascending phase (Fig. 3E,  $n=270$  interneurons,  $p=4 \times 10^{-11}$ ). Jointly these data suggest that the pattern-specific coactivation of interneurons with individual assembly patterns provides a mechanism to support the segregation of assemblies during the descending phase of RRO.

### **Phase-specific recruitment of interneurons by assembly neurons**

Finally, we asked which mechanisms might mediate the enhanced assembly-recruitment of interneurons during descending RRO. One possibility would be that interneurons become more responsive to local glutamatergic drive from assembly neurons. To directly test this hypothesis, we analyzed putative excitatory synaptic connections from pyramidal cells onto interneurons using spike train cross-correlation (English et al., 2017). In total, we detected 234 connections (Fig. 4A,  $n=13$  mice, 14842 connections tested). During the descending phase of RRO, spike transmission probability was significantly increased compared to the ascending phase (Fig. 4B,  $n=204$  synaptic interactions,  $p=0.009$ ). To directly compare assembly and non-assembly neurons, we separated the data set in connections from pyramidal neurons with high weight in at least one pattern in the recording (assembly connections, ~39% of connections) or low weight (non-assembly connections, 61% of connections). Both types of connections did not differ in their overall spike transmission (Fig. 4C,  $p=0.532$ ), connection probability, or convergence (Supplementary Fig. 5). However, while non-assembly connections showed indistinguishable spike transmission when analysed separately for the ascending and descending phase of RRO (Fig. 4D,  $n=122$ ,  $p=0.222$ ), assembly connections displayed stronger spike transmission probability during the descending phase (Fig. 4D,  $n=82$ ,  $p=0.003$ ). These data jointly suggest that RROs support sparse assembly activity during the descending phase of each cycle by defining time windows of enhanced responsiveness of the local interneuron population to excitatory drive from assembly neurons.

## 164 Discussion

165 We found that spontaneously occurring assemblies in the mPFC align their activation with the  
166 descending phase of ongoing RRO. We provide evidence that this effect is explained by an  
167 emergent property of the circuit rather than the simple combination of RRO-coupled neurons into  
168 assemblies. This implies that RROs might have a stronger pacemaking effect on neuronal circuits  
169 than previously assumed on the basis of recordings from individual neurons.

170 A technical limitation when studying neuronal assemblies is the unequivocal identification of  
171 time points of assembly onset. Incomplete sampling of the local neuron population and  
172 thresholding the assembly expression time course, as done in our study and others (van de Ven et  
173 al., 2016, El-Gaby et al., 2021), might underestimate the real number of active assemblies at any  
174 given time point. However, our key finding that RROs define time windows of preferred assembly  
175 activation did hold for different activation thresholds, suggesting that the RRO modulation does not  
176 depend on the parameter selection but rather represents a fundamental property of the behaviour  
177 of cortical assemblies. It should be further noted that our method of assembly detection does not  
178 take into account the temporal structure of the neuronal activity in the assemblies, but solely  
179 detects whether or not neurons show significant coactivation. Neuronal assemblies have, however,  
180 also been defined based on the temporal alignment of spikes (i.e. neuronal sequences) in both the  
181 hippocampus (Chenani et al., 2019) and neocortex (Carrillo-Reid et al., 2015, Luczak et al., 2007,  
182 Luczak et al., 2009). Future work will be required to test whether the principle of RR modulation  
183 applies to such neuronal sequences.

184 Our data add to the notion that cell assemblies exist in the absence of specific stimuli,  
185 arguing in favor of pre-existing network structure suitable to integrate new information using a pool  
186 of readily available network motifs (Miller et al., 2014, Almeida-Filho et al., 2014, Carrillo-Reid et  
187 al., 2015, Hamm et al., 2017, Dejean et al., 2016). While assembly activity was higher during the  
188 descending RRO phase, the overlap between individual assemblies was reduced during that time  
189 (Fig. 3A). These data imply that the co-activation of assemblies is actively suppressed during the  
190 descending phase of RR, as the higher frequency of assembly activation would make random  
191 coactivity more likely. The simultaneous recruitment of putative GABAergic interneurons, which



happens distinctly for different assembly patterns, provides a potential mechanism how individual assemblies might separate their activation from each other (Buzsáki, 2010). These data are in agreement with results from the hippocampus showing that GABAergic neurons differentially align their firing with cell assemblies representing distinct places during spatial learning (Dupret et al., 2013). In line with this hypothesis, interneurons were recruited more strongly to assemblies during the descending phase of RRO (Fig. 3E). Importantly, although occurring on the basis of higher interneurons rates during descending RRO, the enhanced interneuron recruitment was not merely an effect of higher interneuron firing since our measure of assembly-aligned recruitment takes into account the local rate before assembly onset. The association of interneuron firing with assemblies could be caused by an enhanced excitability state due to impinging respiration-driven excitation linked with negative LFP deflections in combination with short-term plasticity processes. To lines of evidence argue in favor of this hypothesis: First, using a cross-correlation-based estimation of spike transmission probability, we show that interneurons are particularly receptive to incoming excitatory signals from assembly neurons (Fig. 4D). Presynaptic cooperativity could synergistically impact spike transmission at assembly neuron-interneuron connections: In the hippocampus, synchronized presynaptic activity leads to enhanced spike transmission (English et al., 2017). Such synchronization would be expected for assembly neurons and might thus contribute to higher spike transmission during the descending phase of RROs. Second, interneurons have been shown to be particularly receptive to respiration-driven input. They are consistently found to be more likely to be phase-coupled to RRO than principal cells (Karalis and Sirota, 2018, Biskamp et al., 2017). Furthermore, whole-cell recordings from pyramidal cells in the parietal cortex revealed subthreshold respiration-synchronous membrane potential oscillations likely reflecting GABAergic synaptic currents (Jung et al., 2019). These findings imply that the main effect of respiration-driven inputs to neocortical circuits is mediated through GABAergic neurons.

Our results add to the increasing recognition of internally generated bodily influences as modulators of brain activity and cognitive functions, including drive from respiration, heart rate and gastrointestinal rhythms (Heck et al., 2019, Azzalini et al., 2019). RROs have been directly observed in various areas of the neocortex, hippocampus, thalamus, and amygdala (Zhong et al.,



2017, Ito et al., 2014, Biskamp et al., 2017, Nguyen Chi et al., 2016, Lockmann et al., 2016, Moberly et al., 2018, Jung et al., 2019, Bagur et al., 2021) and are thought to impact cortical circuits through the entrainment of brain oscillations involved in cognitive functions, including theta (Zelano et al., 2016), gamma (Zhong et al., 2017, Biskamp et al., 2017) and sharp-wave/ripple oscillations (Liu et al., 2017). Based on our results we propose that the role of RROs extends to the building blocks of cortical computations, the assemblies. The synchronization of assemblies to RROs might provide an effective sender-reader interaction such that the impact of synchronized activity from upstream can be efficiently interpreted by downstream reader implementations across neocortex and subcortical structures (Buzsáki, 2010). Alternatively, pooling sparse assembly activations in the descending phase of RRO might provide a mechanism to facilitate spontaneous assembly reactivations during offline states, which has been argued to support memory persistence in the presence of synaptic turnover (Fauth and van Rossum, 2019).

## Acknowledgements

This work was supported by the German Research Foundation (grant SA 3609/1-1 to J.-F.S) and by institutional funding (Institute of Physiology I).

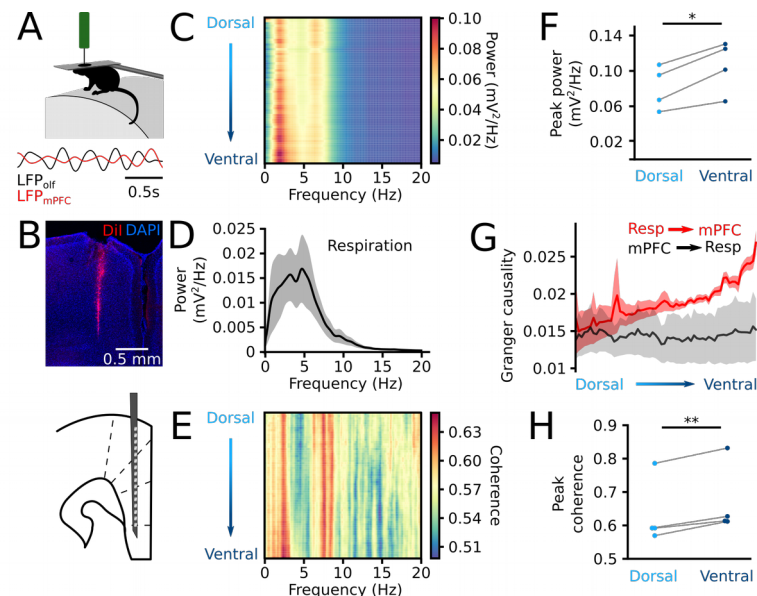
## Author contributions

S.F. and J.-F.S. performed experiments, analyzed data, and wrote the manuscript. J.-F.S. designed the study.

## Declaration of interests

The authors declare no competing interests

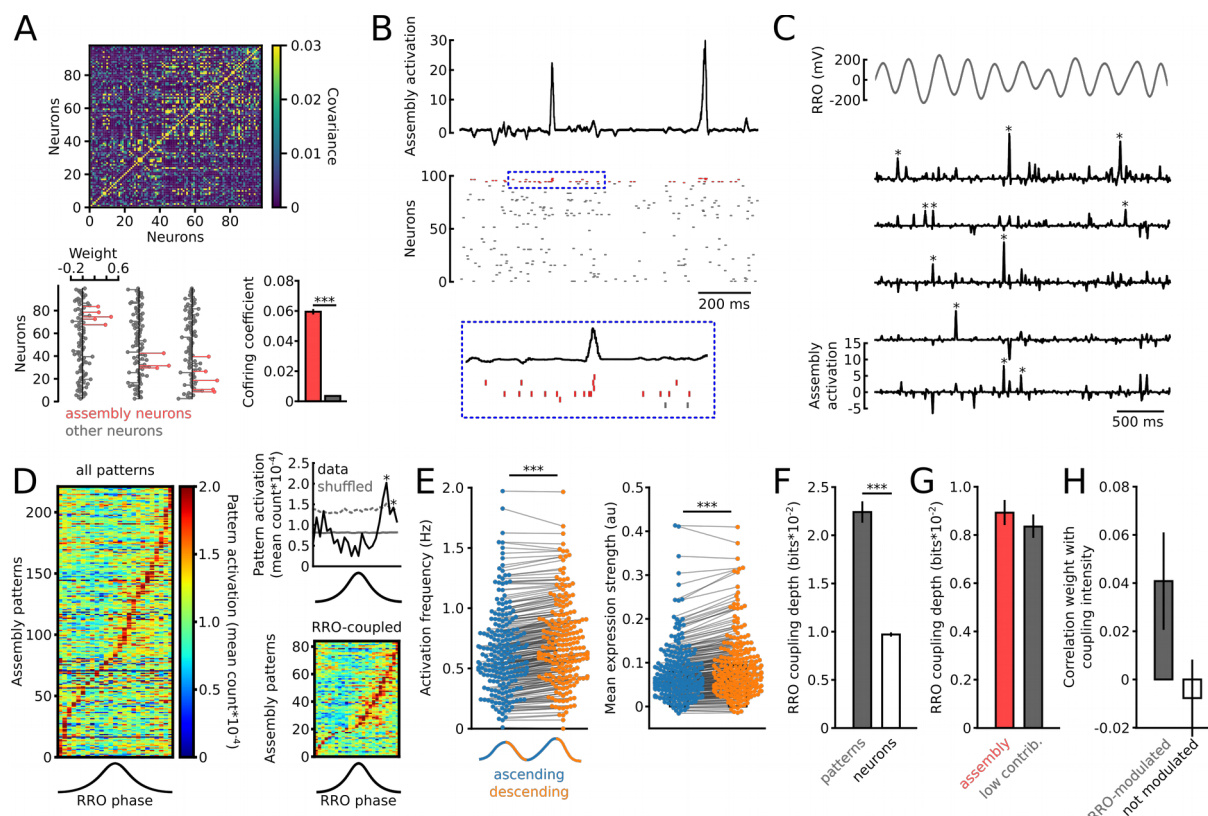
## 243 Figures and figure legends



244 **Fig. 1: The mPFC LFP is entrained by respiration during immobility.**

245 A: Head-fixed mice were recorded during spontaneous immobility, bottom: example traces of the  
 246 olfactory epithelium LFP (black) and the LFP in the mPFC (red) band pass filtered 1-4 Hz during  
 247 immobility. B: Top, coronal section of the mPFC showing the shank of the silicon probe. Bottom:  
 248 schematic of the recording configuration in the mPFC. C: Mean power spectral density of the  
 249 mPFC along the dorso-ventral axis. D: Power spectral density of the olfactory epithelium LFP  
 250 (shaded area: sem). E: Mean coherence between the mPFC and the respiration along the dorso-  
 251 ventral axis. F: Amplitude of the peak power for the most dorsal and ventral recording sites.  
 252  $P=0.014$ . G: Depth profile of the Granger causality of the mPFC by the respiration (red) and of the  
 253 respiration by the mPFC (black). H: Peak coherence between the respiration and the mPFC LFP  
 254 for the most dorsal and ventral recording sites.  $n=4$  mice,  $p=0.007$ . \*  $p<0.05$ , \*\*  $p<0.01$ , paired  $t$ -  
 255 tests.

256



258 **Fig. 2: Cell assemblies preferentially activate during the descending phase of RROs.**

259 A: Assemblies were extracted from covariance matrices of binned spike trains. Top, the example  
260 covariance matrix of simultaneously recorded pyramidal cells in one session. Bottom, examples of  
261 three assembly weight vectors with assembly neurons labelled in red. Assembly neurons showed  
262 stronger cofiring than other neurons, confirming their joint assembly membership.  $n=674$  assembly  
263 and 454206 other pairs,  $p=10^{-131}$ . B: Time course of activation of the first assembly pattern shown  
264 in A along with the pyramidal cells giving rise to the pattern. The inset in the blue box shows one  
265 activation at higher resolution. C: Examples of assembly activations (asterisks) with simultaneously  
266 recorded RRO (1-5 Hz-filtered) during immobility. D: Average assembly activation frequency as a  
267 function of RRO phase revealed preferential occurrence of assemblies during the descending  
268 phase. Right: Example (top) and summary (bottom) of significantly RRO-entrained assemblies. E:  
269 Average pattern frequency (left) and expression strength (right) during the ascending and  
270 descending phase.  $n=221$ ,  $p=4.8 \times 10^{-11}$  and  $p=6.0 \times 10^{-6}$  paired  $t$ -tests. F: RRO-coupling strengths of  
271 assemblies and all individual pyramidal neurons.  $n=221$  and 1145,  $p=6 \times 10^{-20}$ . G: Assembly neurons

272 and cells with low contribution to a pattern showed similar RRO-coupling depth.  $n=142$  and 143  
 273 patterns,  $p=0.648$ . H: Similar correlation between weight in an assembly pattern and RRO coupling  
 274 intensity for RRO-modulated ( $n=84$ ) and non-modulated patterns ( $n=137$ ).  $p=0.063$ . \*\*\*  $p<0.001$ ,  
 275 Welch's tests. Data are shown as mean  $\pm$  sem.

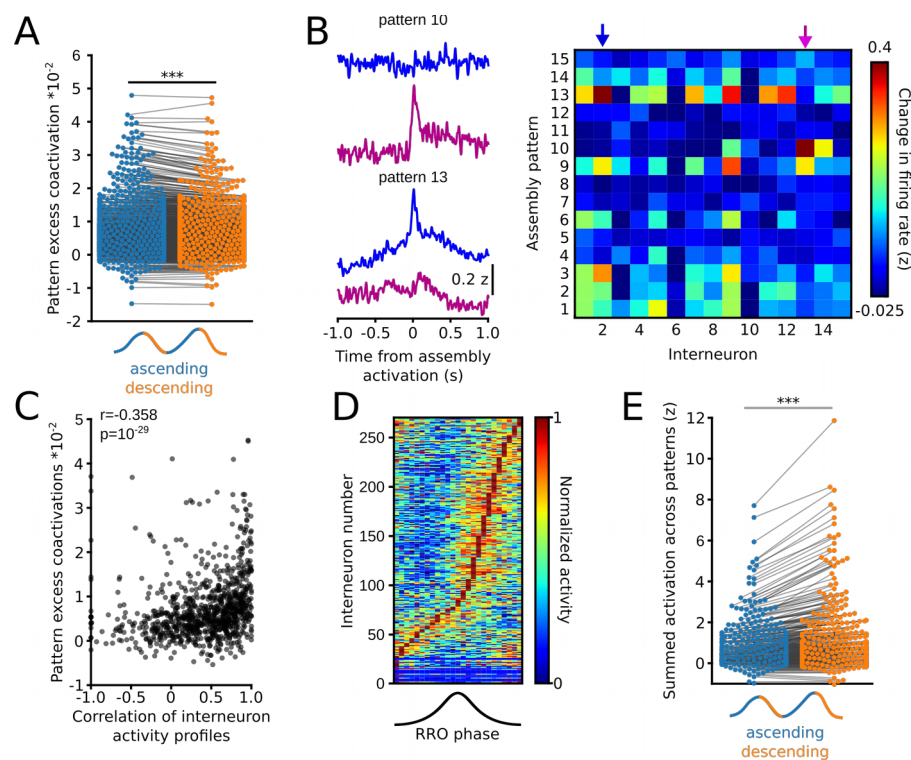


**Fig. 3: RRO phase-specific alignment of interneurons with assemblies.**

A: Quantification of coactivation of assembly patterns within  $\pm 10$  ms revealed reduced coactivation frequency during the descending phase of ongoing RRO.  $n = 931$  pairs,  $p = 0.004$ . B: Interneurons show differential activation profiles in relation to patterns. Left: example normalized firing rate of two interneurons (purple and blue) relative to the onset of two different assembly patterns (pattern 10 and 13). Right: Interneuron profile matrix summarizing the normalized firing change of all interneurons in the recording in response to the onset of all patterns in one session. Arrows indicate the interneurons shown on the left. C: Correlation of pattern coactivation strength and similarity of the interneuron profile of the same patterns.  $n = 13$  mice. D: Interneurons align their firing to the descending phase of RRO. E: Interneuron recruitment by assemblies is enhanced during descending RRO. The graph shows the summed normalized activation of each interneuron to all patterns.  $n = 270$  interneurons,  $p = 6 \times 10^{-11}$ . Paired  $t$ -tests.

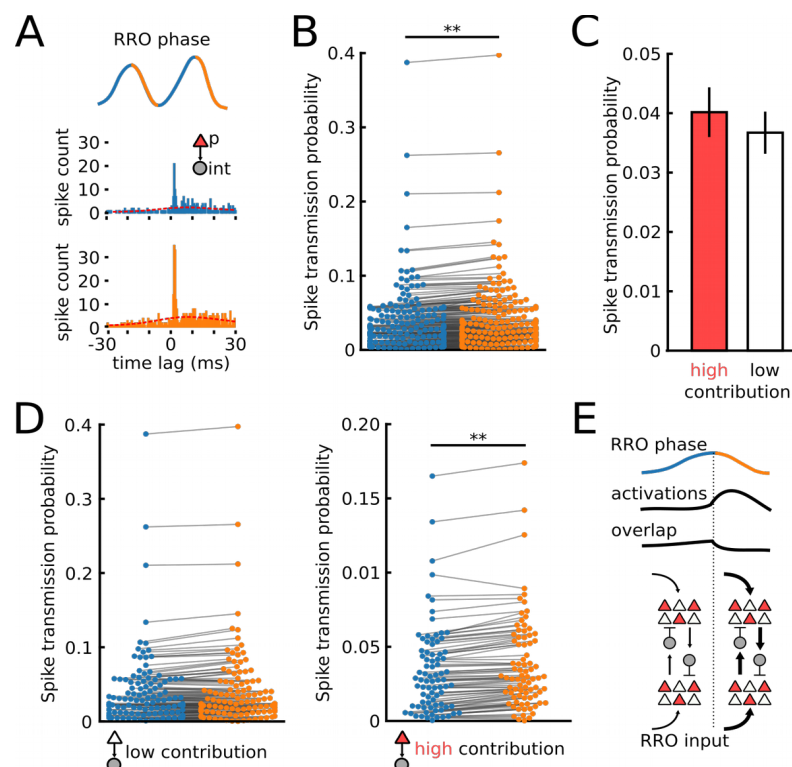


**Fig. 4: RRO phase-specific recruitment of interneurons by assembly neurons.**

A. Example of spike transmission at a pyramidal cell (p)-interneuron (int) connection during the ascending (blue) and descending phase of RRO (orange). Red line indicates the slowly comodulated baseline. B: Summary of connection strength during ascending and descending RRP phase. Spike transmission was significantly enhanced during the descending phase.  $n=204$  connections,  $p=0.009$ . C: Unaltered overall spike transmission probability at assembly neuron-interneuron (high contribution,  $n=91$ ) and non-assembly-interneuron connections (low contribution,  $n=143$ ,  $p=0.532$ , Welch's test). D: Spike transmission for non-assembly neuron-to-interneuron connections did not depend on RRO phase (left,  $n=122$ ,  $p=0.222$ ) while connections from assembly neurons displayed stronger transmission during descending RRO (right,  $n=82$ ,  $p=0.0027$ ). E: Schematic of the proposed function of RRO: Assembly activations are favoured during the descending phase, while assembly overlap is minimized due to the enhanced recruitment of interneurons.  $**p<0.01$ . Data in C are shown as mean  $\pm$  sem. Paired  $t$ -tests unless indicated otherwise.

## 303 **Methods**

### 304 Mice

305 C57Bl6/J mice of both sexes were used in this study. The animals had free access to food and  
 306 water and were maintained on a 12 dark/light cycle. Mice were 6 to 13 weeks old. All experiments  
 307 were performed in agreement with national legislation and were approved by the  
 308 Regierungspräsidium Freiburg. We analyzed data from 10 mice that were recorded in the context  
 309 of a previous study (Sauer and Bartos, 2021). 4 additional mice were implanted and recorded for  
 310 this study.

### 312 Surgical procedures

313 A stainless steel head plate was implanted on the skull under general anesthesia in isoflurane  
 314 (induction: 3%, maintenance: 1-2%) using dental cement. In 4 mice, a 0.8 mm hole was drilled  
 315 above the nasal cavity, and a silver wire insulated up to ~0.5 mm from the extremity was inserted  
 316 between the olfactory epithelium and the bone, and cemented in place. The animals were allowed  
 317 to recover from head plate implantation for at least three days. Buprenorphin (0.1 mg/kg body  
 318 weight) and Carprofen (5 mg/kg body weight) were injected subcutaneously before the surgery for  
 319 pain relief. Once the animals were habituated to head-fixation (see below), a craniotomy was  
 320 performed over both mPFCs (1.9 mm anterior, 0.4 mm lateral of bregma) under isoflurane  
 321 anesthesia. The craniotomy was then covered with a drop of phosphate-buffered saline (PBS) and  
 322 sealed of with QuikCast elastomer until the recordings took place. An additional injection of  
 323 Carprofen was given for analgesia prior to craniotomy.

### 325 Single-unit recording in the virtual reality

326 The mice were habituated to running on a circular track in a virtual reality. For head fixation, the  
 327 mice were briefly anesthetized in isoflurane (3% in O<sub>2</sub>). During habituation and recording, the mice  
 328 ran on a circular styrofoam wheel. First, animals were habituated to head-fixation for at least three  
 329 days without the virtual reality turned on. Then, they were daily exposed to the virtual reality  
 330 (circular track, length 2-3 m, with visual cues placed outside the arena). The virtual reality was



constructed with open-source 3D rendering software Blender (Schmidt-Hieber and Häusser, 2013) and was projected on five computer screens surrounding the head-fixation setup.

Recordings were performed 1-3 days after the craniotomy using H3 single-shank silicon probes (64 recording sites spaced 20  $\mu\text{m}$  apart, total shank length 1275  $\mu\text{m}$ , Cambridge Neurotech). The probe was coated with a fluorescent marker (DiI or DiO) and was slowly ( $\sim 2\text{-}5\ \mu\text{m/s}$ ) lowered to the mPFC (1600-1900  $\mu\text{m}$  below brain surface). The probe was left in place before the recordings for 10-15 min. Wide-band signals were recorded with a 64-channel amplifier (Intan Technologies) using OpenEphys GUI software (30 kHz sampling frequency). Movement of the animal was assessed by recording the motion of the running wheel as a pulse-width modulated signal. After the recording, the probe was slowly retracted and the craniotomy sealed off with QuickCast elastomer. With each mouse, 1-3 recording sessions were performed (1 session per day).

## Histology

After recording, the animals were deeply anesthetized with ketamin/xylazine (i.p. injection) and transcardially perfused with  $\sim 20\ \text{ml}$  phosphate-buffered saline followed by  $\sim 30\ \text{ml}$  of 4% paraformaldehyde. 100  $\mu\text{m}$ -thick coronal sections of the mPFC were cut after post-fixation in fixative overnight at  $4^\circ$ . The slices were washed in PBS and stained with 4',6-diamidino-2-phenylindole. A laser scanning microscope (LSM 710 or 900, Zeiss) was used to visualize the location of the silicon probe. Recording locations ranged from layer 2 to 6, spanning from the accessory motor cortex to the medial orbital area.

## Single-unit isolation

Single units were extracted from bandpass-filtered data (0.3-3 kHz) using MountainSort (Chung et al., 2017). Putative single-unit clusters with high isolation index ( $>0.90$ ) and low noise overlap ( $<0.1$ ) were kept for manual curation, during which only clusters with a clear refractory period were kept. In case of two clusters with similar waveforms, cross-correlation was used to assess whether clusters had to be merged. Isolated units were separated in putative excitatory and inhibitory

neurons based on trough-to-peak duration and asymmetry index as described before (Sirota et al., 2008).

### Analysis of respiration-local field potential coupling

Olfactory epithelium and mPFC LFP power spectral density and cross spectral density were computed using Welch's average periodogram method. For the power, the signals were divided in Hann windows of 2 s length with no overlap and padded by a factor 10, and the obtained power spectral density was then averaged across windows. The coherence was computed on windows of 4 s as the normalized cross spectral density of 2 s Hann windows with no overlap and then averaged. The Granger causality was defined as the variance of the residual from a linear autoregressive model fitted on a 2 s window of the mPFC LFP or the LFP<sub>olf</sub> divided by the residual of a vector autoregressive model including the LFP<sub>olf</sub> or the mPFC LFP. Both autoregressive and vector autoregressive models (from the *statsmodels* python package) had a fixed lag of 1, and were computed on signals filtered below 50 Hz and downsampled to 100 Hz.

### Detection of assembly patterns

Assembly extraction was performed using principal- and independent component analysis following a published procedure using simultaneously recorded pyramidal cells (van de Ven et al., 2016). The extraction was done on the entire recording duration, including movement and immobility, while the analysis of assembly activations in relation to ongoing RROs was performed during immobility. We used a total of 13 mice with sufficient immobility duration for this analysis.

The spike trains of  $n$  pyramidal neurons were binned in  $B$  25 ms bins and normalized by z-scoring to avoid bias by highly active neurons. To detect the number of assembly patterns in a recording, principal component analysis was applied to the binned spike train matrix. We next used the Marčenko-Pastur law to extract the number of significant assembly patterns (Marčenko and Pastur, 1967, Lopes-dos-Santos et al., 2013). The Marčenko-Pastur law indicates that a correlation matrix constructed from independent random variables yields eigenvalues below a critical value  $c$  given as

$$c = \left(1 + \sqrt{\frac{n}{B}}\right)^2.$$

If neurons fire correlated with each other (as it would be the case for assemblies), eigenvalues above the critical limit will exist. The number of eigenvalues exceeding the theoretical limit thus indicates the number of assembly patterns (Lopes-dos-Santos et al., 2013). Independent component analysis was then used to extract activity patterns that are as independent from each other as possible. Using the fastICA algorithm of *scikit.learn*, we extracted the number of independent components given by the eigenvalues above  $c$ . The resulting components represent the weight vectors of each assembly pattern. Note that the orientation of independent components is arbitrary, so each vector was oriented to have the largest deflection in positive direction and was further scaled to unit length. Assembly neurons were defined as those cells with a weight exceeding 2x the standard deviation of the pattern vector (van de Ven et al., 2016). Sparsity of assembly patterns (i.e. to what extent assemblies were dominated by high weights of few neurons) was quantified as

$$1 - \frac{\sqrt{n} - \sum |k_i|}{\sqrt{n} - 1},$$

where  $n$  denotes the length of the weight vector, and  $k_i$  is the weight of neuron  $i$  in pattern  $k$ .

### Reconstruction of assembly activations over time

To obtain the assembly activation time course  $T$  for all  $k$  patterns at high resolution, the weight vectors corresponding to the assemblies were projected on smoothed spike trains  $z$  of all neurons:

$$T_p(t) = z(t)^T P_k z(t),$$

where  $T$  denotes the transpose operator and  $P_k$  gives the outer product of the  $k^{\text{th}}$  weight vector. The spike train matrix  $z$  was constructed by convolving each neuron's spike train with a Gaussian kernel (standard deviation 7.2 ms). This procedure resulted in smooth time courses of pattern activation. We set a threshold of 5 to detect assembly activations, unless indicated otherwise (van de Ven et al., 2016).

### 413 Assembly detection in simulated data

414 A simulated binned spike train matrix  $B_{sim}$  consisting of 70 neurons and 1000 bins was constructed  
 415 as 70 Poisson neurons using the *numpy.random.poisson* function (with lam=1). Assemblies were  
 416 modeled as a group of neurons with joint elevation in spike rate in 50 randomly chosen bins. The  
 417 spike rate increase was modeled by randomly drawing a spike value ranging between 0 and 6 for  
 418 each of the assembly neurons. This way, the identity of the assembly neurons was known a priori,  
 419 while the time points of activation were not. The assembly extraction procedure was applied as  
 420 described above, except that the reconstruction of the time course of the assemblies was done  
 421 directly on  $B_{sim}$  rather than convolved spike trains.

### 423 Single-neuron analysis

424 The cofiring coefficient was calculated using Pearson's correlation coefficient from binned spike  
 425 trains (25 ms bin width) in a round-robin fashion separately for assembly and non-assembly  
 426 neurons. To assess the spatial extent of assemblies, we measured for each pattern the average  
 427 distance between all assembly neurons and a matching number of randomly drawn neurons. The  
 428 position of the neuron was defined by the electrode with largest negative voltage deflection. RRO-  
 429 coupling of units was quantified using the Kullback-Leibler distance (see below). Only cells with at  
 430 least 200 spikes during the immobility epochs were considered for this analysis. To compare RRO-  
 431 coupling for assembly and non-assembly neurons, the coupling value of assembly neurons for  
 432 each pattern was compared with a matching number of low-contributing neurons (i.e. with the  
 433 lowest weights in the pattern vector). The association of interneurons with assembly patterns was  
 434 tested by first z-scoring the convolved interneuron spike trains. Then, the mean firing rate change  
 435 during a 30 ms window following assembly onset relative to preceding baseline (833 ms long,  
 436 ending 166 ms before assembly onset) was calculated for each pattern and interneuron.

### 438 Assembly analysis

439 Assembly-RRO coupling was assessed by extracting first the times of assembly activations by  
 440 threshold-crossing. After an onset was detected, no further activations could be scored for 50 ms to

avoid double-detection. Then, for each activation we determined the instantaneous phase of the ongoing 1-5 Hz filtered and Hilbert-transformed RRO, and quantified the mean activation as a function of RRO phase bins (25 bins). This coupling measure thus carries the unit “mean activations/14.4°”. Coupling strength was expressed with the Kullback-Leibler distance  $K$  between the actual phase distribution  $P$  and a uniform distribution  $U$  with the same mean:

$$K = \sum_{b=1}^n P_b \log_{10} \left( \frac{P_b}{U_b} \right),$$

where  $n$  denotes the bin number. Significant coupling was tested by randomly shuffling the activation times (1000 iterations). Phase-coupling was considered significant when  $K$  exceeded the 99<sup>th</sup> percentile of the random distribution. Kullback-Leibler distance was also used to obtain phase-coupling of single-units.

#### Assembly coactivation and synaptic interactions

To detect assembly coactivations and putative pyramidal cell-interneuron connections, we used a cross-correlation based framework (English et al., 2017). For synaptic connections, we first determined the raw cross-correlation between two binned spike trains (0.4 ms bins) for neurons with more than 500 spikes using the `filter_correlogram` function of the *neuronpy.util.spiketrain* package. Criteria for a significant monosynaptic interaction were a peak in the monosynaptic time window (0.8-2.8 ms following the spike in the pyramidal cell) significantly exceeding the co-modulated baseline and the peak in anti-causal direction (i.e. interneuron-pyramidal cell, -2 to 0 ms). The baseline  $b$  was obtained by convolving the raw cross-correlogram with a partially hollowed Gaussian function (hollow fraction: 0.6, standard deviation: 10 ms). The Poisson distribution with continuity correction was used to estimate the probability of the observed magnitude of cross-correlation in the monosynaptic bins ( $P_{syn}$ ),

$$P_{syn} = 1 - \sum_{x=0}^{n-1} \left( \frac{e^{-b(m)} b(m)^x}{x!} \right) - 0.5 \frac{e^{-b(m)} b(m)^n}{n!}.$$

Similarly, we estimated the probability of the observed count in the monosynaptic bins of the cross-correlogram being larger than the count in anticausal direction ( $c_{\text{anticausal}}$ ) using the Poisson distribution with continuity correction,

$$P_{\text{causal}} = 1 - \sum_{x=0}^{n-1} \left( \frac{e^{-c_{\text{anticausal}}} c_{\text{anticausal}}^x}{x!} \right) - 0.5 \left( \frac{e^{-c_{\text{anticausal}}} c_{\text{anticausal}}^n}{n!} \right).$$

Following optogenetic ground truth data obtained in the hippocampus, a pair was marked as connected if  $P_{\text{syn}} < 0.001$  and  $P_{\text{causal}} < 0.0026$  (English et al., 2017). Spike transmission probability was defined as the spiking in the monosynaptic window exceeding  $b$  normalized by the number of presynaptic spikes. For all significantly connected pairs, we additionally extracted spike transmission probability separately for the ascending and descending phases of RRO, which were defined from 1-5 Hz filtered and Hilbert-transformed raw LFP traces. Only connections with positive spike transmission during both ascending and descending phase were considered for this analysis. Convergence was assessed by taking the number of convergent connections divided by the number of total connections of the session. This analysis was only applied to sessions with at least 3 connections (12 sessions from 10 mice). For assembly coactivations, the coactivation strength was determined by summing the values exceeding  $b$  in the -10 to + 10 ms time window for all pairs of patterns.

## Statistical analysis

Unpaired comparisons were done with two-sided Welch's tests, which is robust against deviation from normal distribution at large sample sizes (Stonehouse and Forrester, 1998). For small group sizes  $< 15$ , an unpaired two-sided  $t$ -test was used. Correlations were assessed with Spearman's correlation coefficient. Pairwise comparisons were done with a paired  $t$ -test. Data are presented as full data ranges or as mean  $\pm$  sem where indicated. All analysis (except for initial spike sorting) were performed in Python2.7.

## 489 References

- Almeida-Filho DG, Lopes-dos-Santos V, Vasconcelos NAP, Miranda JGV, Tort ABL, Ribeiro S. 2014. An investigation of Hebbian phase sequences as assembly graphs. *Front Neural Circuits* **8**. doi:10.3389/fncir.2014.00034
- Arshamian A, Iravani B, Majid A, Lundström JN. 2018. Respiration Modulates Olfactory Memory Consolidation in Humans. *J Neurosci* **38**:10286–10294. doi:10.1523/JNEUROSCI.3360-17.2018
- Azzalini D, Rebollo I, Tallon-Baudry C. 2019. Visceral Signals Shape Brain Dynamics and Cognition. *Trends in Cognitive Sciences* **23**:488–509. doi:10.1016/j.tics.2019.03.007
- Bagur S, Lefort JM, Lacroix MM, de Lavilléon G, Herry C, Chouvaeff M, Billand C, Geoffroy H, Benchenane K. 2021. Breathing-driven prefrontal oscillations regulate maintenance of conditioned-fear evoked freezing independently of initiation. *Nat Commun* **12**:2605. doi:10.1038/s41467-021-22798-6
- Biskamp J, Bartos M, Sauer J-F. 2017. Organization of prefrontal network activity by respiration-related oscillations. *Sci Rep* **7**:45508. doi:10.1038/srep45508
- Buzsáki G. 2010. Neural syntax: cell assemblies, synapsembles, and readers. *Neuron* **68**:362–385. doi:10.1016/j.neuron.2010.09.023
- Carrillo-Reid L, Miller JK, Hamm JP, Jackson J, Yuste R. 2015. Endogenous Sequential Cortical Activity Evoked by Visual Stimuli. *J Neurosci* **35**:8813–8828. doi:10.1523/JNEUROSCI.5214-14.2015
- Chenani A, Sabariego M, Schlesiger MI, Leutgeb JK, Leutgeb S, Leibold C. 2019. Hippocampal CA1 replay becomes less prominent but more rigid without inputs from medial entorhinal cortex. *Nature Communications* **10**:1341. doi:10.1038/s41467-019-09280-0
- Chung JE, Magland JF, Barnett AH, Tolosa VM, Tooker AC, Lee KY, Shah KG, Felix SH, Frank LM, Greengard LF. 2017. A Fully Automated Approach to Spike Sorting. *Neuron* **95**:1381–1394.e6. doi:10.1016/j.neuron.2017.08.030
- Dejean C, Courtin J, Karalis N, Chaudun F, Wurtz H, Bienvenu TCM, Herry C. 2016. Prefrontal neuronal assemblies temporally control fear behaviour. *Nature* **535**:420–424. doi:10.1038/nature18630
- Dupret D, O'Neill J, Csicsvari J. 2013. Dynamic reconfiguration of hippocampal interneuron circuits during spatial learning. *Neuron* **78**:166–180. doi:10.1016/j.neuron.2013.01.033
- El-Gaby M, Reeve HM, Lopes-Dos-Santos V, Campo-Urriza N, Perestenko PV, Morley A, Strickland LAM, Lukács IP, Paulsen O, Dupret D. 2021. An emergent neural coactivity code for dynamic memory. *Nat Neurosci* **24**:694–704. doi:10.1038/s41593-021-00820-w
- English DF, McKenzie S, Evans T, Kim K, Yoon E, Buzsáki G. 2017. Pyramidal Cell-Interneuron Circuit Architecture and Dynamics in Hippocampal Networks. *Neuron* **96**:505–520.e7. doi:10.1016/j.neuron.2017.09.033
- Fauth MJ, van Rossum MC. 2019. Self-organized reactivation maintains and reinforces memories despite synaptic turnover. *eLife* **8**:e43717. doi:10.7554/eLife.43717
- Fontanini A, Bower JM. 2006. Slow-waves in the olfactory system: an olfactory perspective on cortical rhythms. *Trends Neurosci* **29**:429–437. doi:10.1016/j.tins.2006.06.013
- Grosmaître X, Santarelli LC, Tan J, Luo M, Ma M. 2007. Dual functions of mammalian olfactory sensory neurons as odor detectors and mechanical sensors. *Nat Neurosci* **10**:348–354. doi:10.1038/nn1856
- Hamm JP, Peterka DS, Gogos JA, Yuste R. 2017. Altered Cortical Ensembles in Mouse Models of Schizophrenia. *Neuron* **94**:153–167.e8. doi:10.1016/j.neuron.2017.03.019
- Harris KD. 2005. Neural signatures of cell assembly organization. *Nat Rev Neurosci* **6**:399–407. doi:10.1038/nrn1669
- Heck DH, Kozma R, Kay LM. 2019. The rhythm of memory: how breathing shapes memory function. *J Neurophysiol* **122**:563–571. doi:10.1152/jn.00200.2019
- Ito J, Roy S, Liu Y, Cao Y, Fletcher M, Lu L, Boughter JD, Grün S, Heck DH. 2014. Whisker barrel cortex delta oscillations and gamma power in the awake mouse are linked to respiration. *Nat Commun* **5**:3572. doi:10.1038/ncomms4572



- Jung F, Yanovsky Y, Brankač J, Tort AB, Draguhn A. 2019. Respiration competes with theta for modulating parietal cortex neurons. *bioRxiv* 707331. doi:10.1101/707331
- Karalis N, Sirota A. 2018. Breathing coordinates limbic network dynamics underlying memory consolidation. *bioRxiv* 392530. doi:10.1101/392530
- Kay LM. 2015. Olfactory system oscillations across phyla. *Curr Opin Neurobiol* **31**:141–147. doi:10.1016/j.conb.2014.10.004
- Koch C, Rapp M, Segev I. 1996. A brief history of time (constants). *Cereb Cortex* **6**:93–101. doi:10.1093/cercor/6.2.93
- Kőszeghy Á, Lasztóczy B, Forro T, Klausberger T. 2018. Spike-Timing of Orbitofrontal Neurons Is Synchronized With Breathing. *Front Cell Neurosci* **12**:105. doi:10.3389/fncel.2018.00105
- Le Merre P, Åhrlund-Richter S, Carlén M. 2021. The mouse prefrontal cortex: Unity in diversity. *Neuron*. doi:10.1016/j.neuron.2021.03.035
- Liu Y, McAfee SS, Heck DH. 2017. Hippocampal sharp-wave ripples in awake mice are entrained by respiration. *Sci Rep* **7**:8950. doi:10.1038/s41598-017-09511-8
- Lockmann ALV, Laplagne DA, Leão RN, Tort ABL. 2016. A Respiration-Coupled Rhythm in the Rat Hippocampus Independent of Theta and Slow Oscillations. *J Neurosci* **36**:5338–5352. doi:10.1523/JNEUROSCI.3452-15.2016
- Lopes-dos-Santos V, Ribeiro S, Tort ABL. 2013. Detecting cell assemblies in large neuronal populations. *J Neurosci Methods* **220**:149–166. doi:10.1016/j.jneumeth.2013.04.010
- Luczak A, Barthó P, Harris KD. 2009. Spontaneous events outline the realm of possible sensory responses in neocortical populations. *Neuron* **62**:413–425. doi:10.1016/j.neuron.2009.03.014
- Luczak A, Barthó P, Marguet SL, Buzsáki G, Harris KD. 2007. Sequential structure of neocortical spontaneous activity in vivo. *PNAS* **104**:347–352. doi:10.1073/pnas.0605643104
- Marčenko VA, Pastur LA. 1967. DISTRIBUTION OF EIGENVALUES FOR SOME SETS OF RANDOM MATRICES. *Math USSR Sb* **1**:457. doi:10.1070/SM1967v001n04ABEH001994
- Miller JK, Ayzenshtat I, Carrillo-Reid L, Yuste R. 2014. Visual stimuli recruit intrinsically generated cortical ensembles. *PNAS* **111**:E4053–E4061. doi:10.1073/pnas.1406077111
- Moberly AH, Schreck M, Bhattarai JP, Zweifel LS, Luo W, Ma M. 2018. Olfactory inputs modulate respiration-related rhythmic activity in the prefrontal cortex and freezing behavior. *Nat Commun* **9**:1528. doi:10.1038/s41467-018-03988-1
- Nakamura NH, Fukunaga M, Oku Y. 2018. Respiratory modulation of cognitive performance during the retrieval process. *PLoS One* **13**:e0204021. doi:10.1371/journal.pone.0204021
- Nguyen Chi V, Müller C, Wolfenstetter T, Yanovsky Y, Draguhn A, Tort ABL, Brankač J. 2016. Hippocampal Respiration-Driven Rhythm Distinct from Theta Oscillations in Awake Mice. *J Neurosci* **36**:162–177. doi:10.1523/JNEUROSCI.2848-15.2016
- Palm G, Knoblauch A, Hauser F, Schüz A. 2014. Cell assemblies in the cerebral cortex. *Biol Cybern* **108**:559–572. doi:10.1007/s00422-014-0596-4
- Papadimitriou CH, Vempala SS, Mitropolsky D, Collins M, Maass W. 2020. Brain computation by assemblies of neurons. *PNAS* **117**:14464–14472. doi:10.1073/pnas.2001893117
- Peyrache A, Khamassi M, Benchenane K, Wiener SI, Battaglia FP. 2009. Replay of rule-learning related neural patterns in the prefrontal cortex during sleep. *Nat Neurosci* **12**:919–926. doi:10.1038/nn.2337
- Sauer J-F, Bartos M. 2021. Topographically organized representation of space and context in the medial prefrontal cortex. *bioRxiv* 2021.06.04.447085. doi:10.1101/2021.06.04.447085
- Schmidt-Hieber C, Häusser M. 2013. Cellular mechanisms of spatial navigation in the medial entorhinal cortex. *Nat Neurosci* **16**:325–331. doi:10.1038/nn.3340
- Sirota A, Montgomery S, Fujisawa S, Isomura Y, Zugaro M, Buzsáki G. 2008. Entrainment of neocortical neurons and gamma oscillations by the hippocampal theta rhythm. *Neuron* **60**:683–697. doi:10.1016/j.neuron.2008.09.014
- Stonehouse JM, Forrester GJ. 1998. Robustness of the t and U tests under combined assumption violations. *Journal of Applied Statistics* **25**:63–74. doi:10.1080/02664769823304
- van de Ven GM, Trouche S, McNamara CG, Allen K, Dupret D. 2016. Hippocampal Offline Reactivation Consolidates Recently Formed Cell Assembly Patterns during Sharp Wave-Ripples. *Neuron* **92**:968–974. doi:10.1016/j.neuron.2016.10.020

- Zelano C, Jiang H, Zhou G, Arora N, Schuele S, Rosenow J, Gottfried JA. 2016. Nasal Respiration Entrain Human Limbic Oscillations and Modulates Cognitive Function. *J Neurosci* **36**:12448–12467. doi:10.1523/JNEUROSCI.2586-16.2016
- Zhong W, Ciatipis M, Wolfenstetter T, Jessberger J, Müller C, Ponsel S, Yanovsky Y, Brankač J, Tort ABL, Draguhn A. 2017. Selective entrainment of gamma subbands by different slow network oscillations. *Proc Natl Acad Sci USA* **114**:4519–4524. doi:10.1073/pnas.1617249114